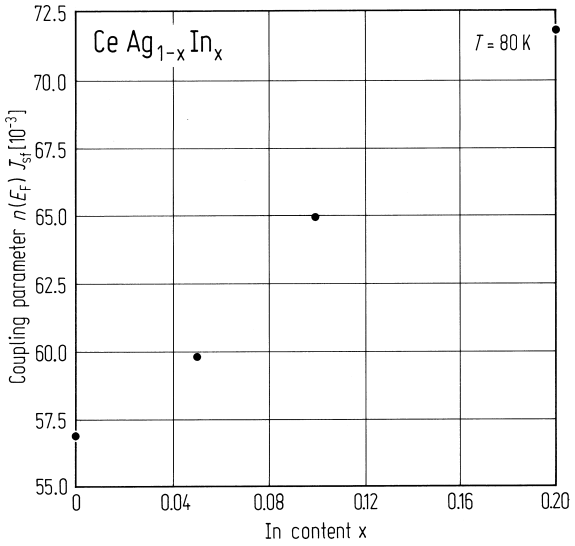

Fig. 238. The k-f coupling parameter $n(E_F)J_{sf}$ as a function of the In concentration x in $CeAg_{1-x}In_x$ [82W1].

1.5.5.5 Phase transitions

Several Heusler alloys, e.g. Ni_2MnGa, Co_2NbSn etc. undergo structural phase transitions at low temperatures. These transitions are believed to be driven by a band Jahn Teller mechanism. As yet there has not been any experimental evidence to confirm this conjecture. Heusler compounds have proved good model systems for studying the dynamics of atomic order. In general Heusler alloys pass from complete random disorder, the A2 structure, through B2 order, the CsCl structure, to the Heusler $L2_1$ arrangement. The A2-B2 ordering temperature is usually denoted by T_2 and the B2-$L2_1$ ordering temperature by T_1.

Heusler alloys in which the magnetic moment is confined to the Mn atom are good local moment systems. In these compounds the manganese moment, which is usually close to 4 μ_B, remains fixed in amplitude when going from the ordered to the paramagnetic state. For these Heusler alloys there is negligible overlap of the Mn d-electron wave functions and the d-band does not participate in the Fermi surface. However, the situation is potentially different for those systems in which the moment is associated with the X atoms or both the X and Y atoms. For such compounds the magnetic atoms are close enough for significant overlap of the d wave function to occur. Hence spin fluctuations may be important. However, thermal expansion measurements have failed to reveal any anomalies at the Curie temperature in Co_2MnZ compounds. This would suggest that the magnetic moments are of fixed amplitude. Similar results were also found in $Ni_{3-x}MnSn$.

Table 53. Melting points of some Heusler alloys [90M1].

Compounds	T_m [°C]
Cu_2MnAl	948
Co_2MnSn	1028
Ni_2MnSn	1125
Ni_2ZrSn	968
Ni_2ZrIn	864

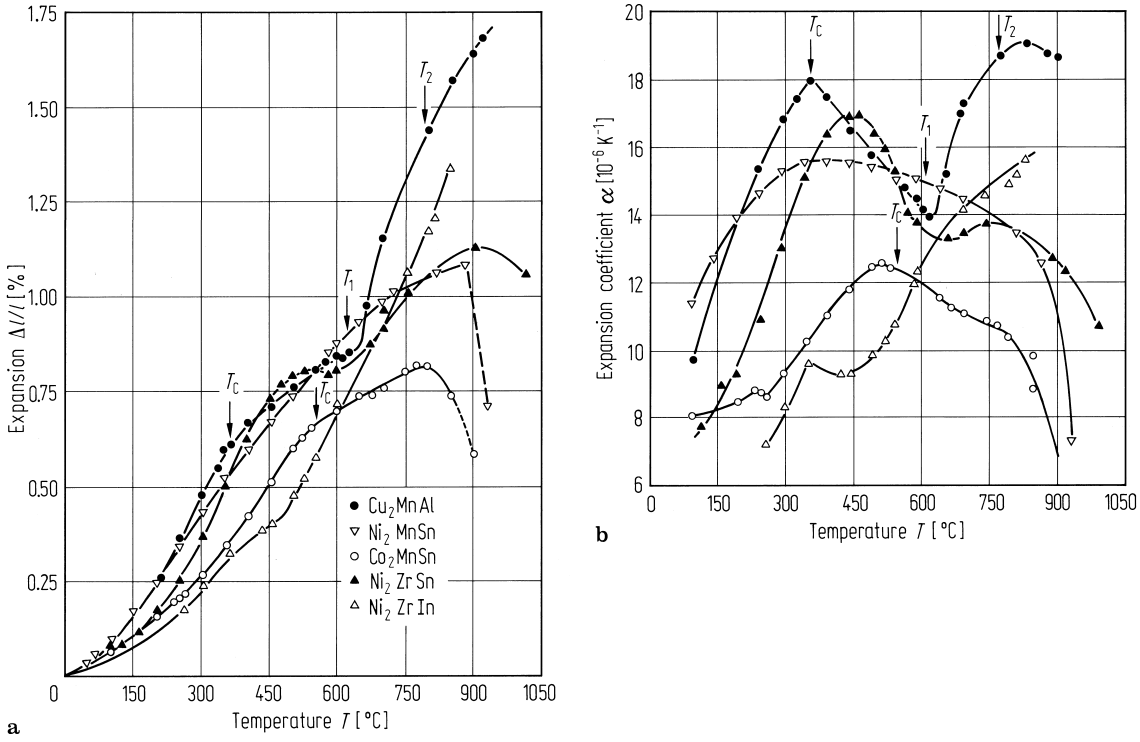

Fig. 239. Dilatometric data for X_2YZ Heusler alloys: (**a**) temperature dependence of the relative thermal expansion $\Delta l/l$; (**b**) temperature dependence of the coefficient of the linear and thermal expansion α [90M1].

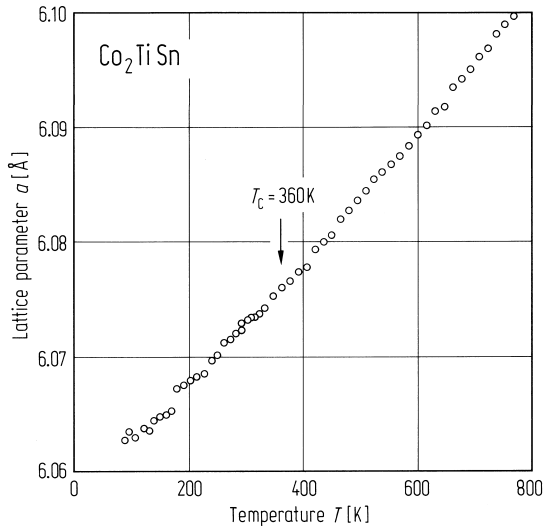

Fig. 240. Temperature dependence of lattice parameter a of Co_2TiSn. The arrow indicates the Curie temperature [92K1].

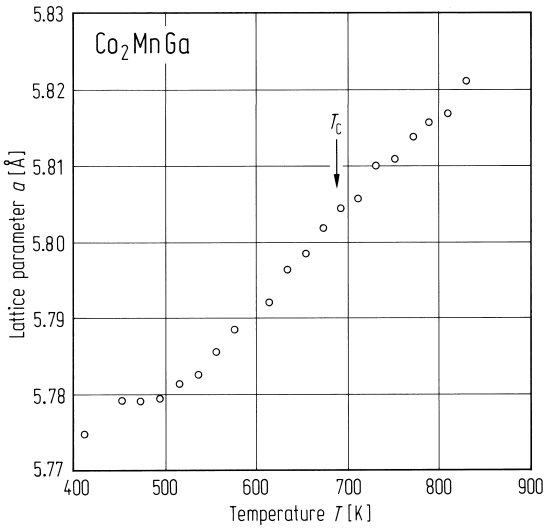

Fig. 241. Temperature dependence of lattice parameter a of Co_2MnGa. The arrow denotes the Curie temperature [88I1].

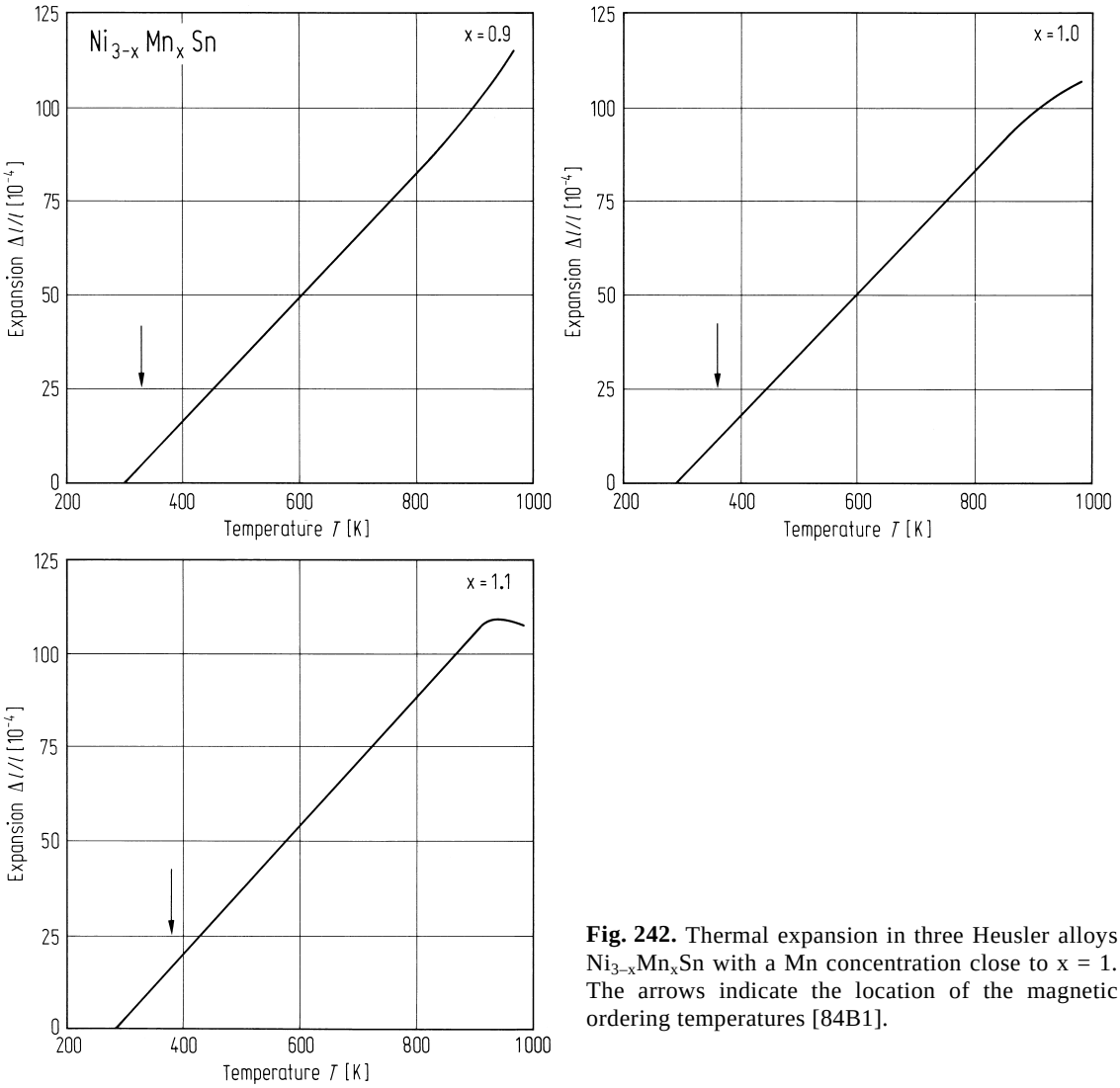

Fig. 242. Thermal expansion in three Heusler alloys $Ni_{3-x}Mn_xSn$ with a Mn concentration close to x = 1. The arrows indicate the location of the magnetic ordering temperatures [84B1].

However, a distinct anomaly occurs at T_C in the $C1_b$ compound PtMnSn, suggesting that the amplitude is not fixed in magnitude. This could occur if the Mn atoms are disordered.

Many of the structural phase transitions are martensitic. Detailed investigations have taken place on both magnetic and non-magnetic systems.

Extensive investigations of the martensitic phase transition in the ferromagnet Ni_2MnGa have been made. This compound transforms martensitically at 202 K to a predominantly tetragonal structure below. There is in fact a modulation of the (110) atomic planes with a periodicity of five atomic layers [88W1]. The transition is accompanied by a strong soft mode behaviour in the transverse acoustic phonon branch with q along the [110] direction and polarisation along [1-10] in the high-temperature phase. Below the transition the system becomes magnetically anisotropic.

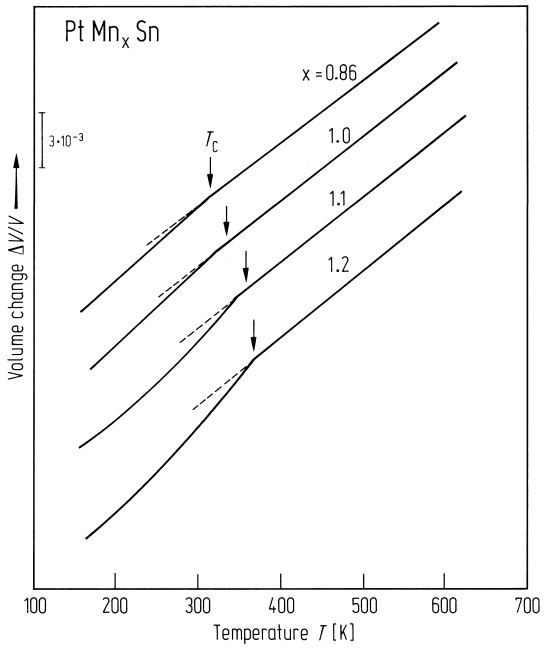

Fig. 243. Relative volume change as a function of temperature for some PtMnSn alloys [83K1].

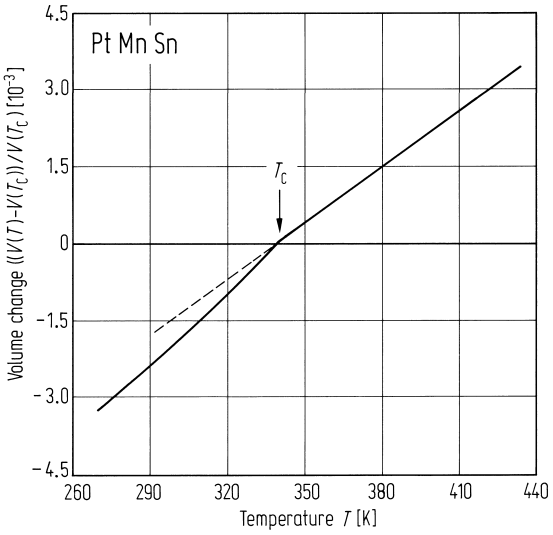

Fig. 244. Reduced volume change as a function of temperature of PtMnSn [83K1].

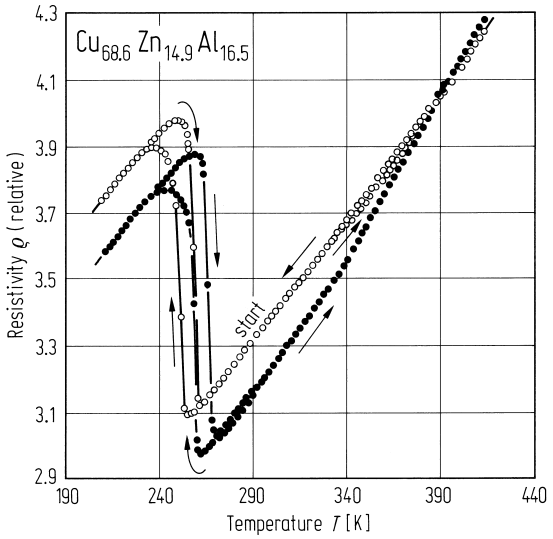

Fig. 245. Electrical resistivity of $Cu_{68.6}Zn_{14.9}Al_{16.5}$ quenched from 923 K indicating a martensitic phase transition [86M1].

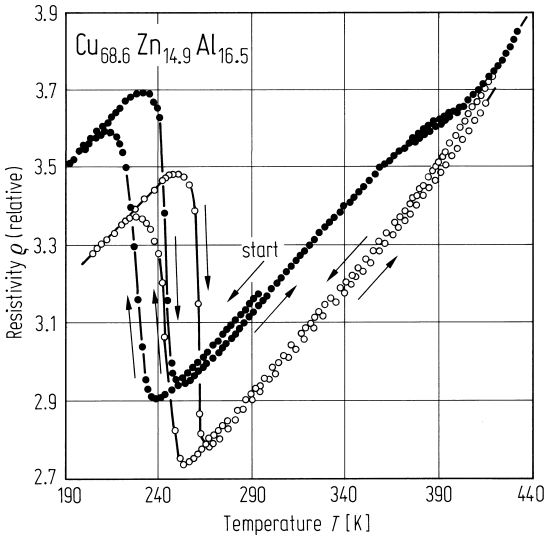

Fig. 246. Electrical resistivity of $Cu_{68.6}Zn_{14.9}Al_{16.5}$ quenched from 513 K indicating a martensitic phase transition [86M1].

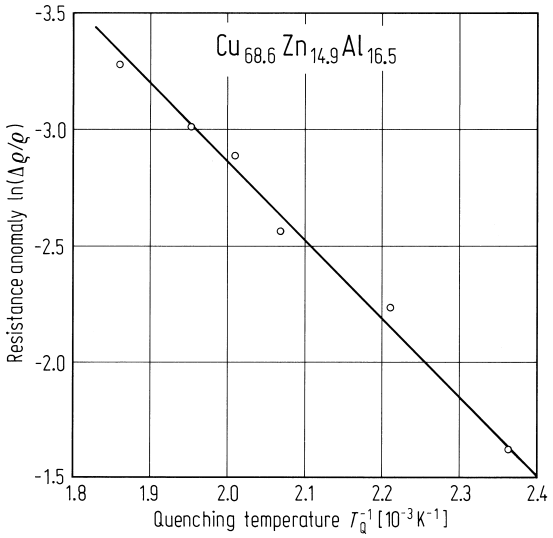

Fig. 247. Logarithm of the magnitude of the electrical resistance anomaly at the phase transition in $Cu_{68.6}Zn_{14.9}Al_{16.5}$ as a function of the reciprocal of the quenching temperature [86M1].

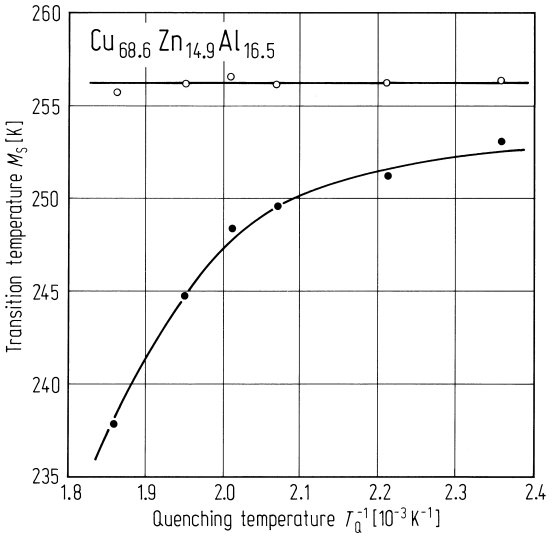

Fig. 248. Start temperature M_s of the martensitic phase transition plotted against the inverse quenching temperature for $Cu_{68.6}Zn_{14.9}Al_{16.5}$. The open and closed circles correspond to the M_s temperature before and after the resistivity anomaly occurs respectively [86M1].

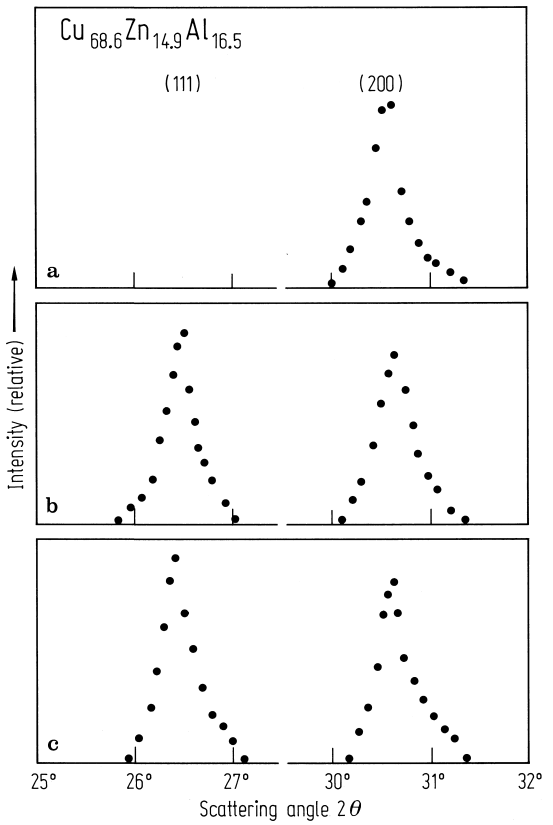

Fig. 249. X-ray diffraction patterns of $Cu_{68.6}Zn_{14.9}Al_{16.5}$ for a specimen (**a**) quenched from 923 K, (**b**) and (**c**) quenched from 513 K before and after the resistance anomaly occurs respectively [86M1].

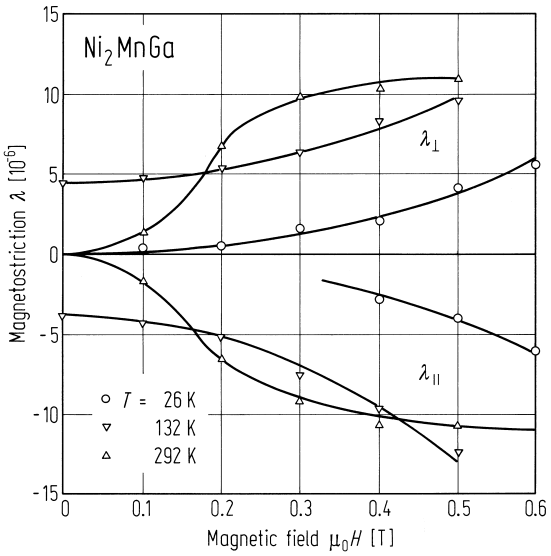

Fig. 251. Magnetostriction in Ni_2MnGa above and below the martensitic phase transition [91D1].

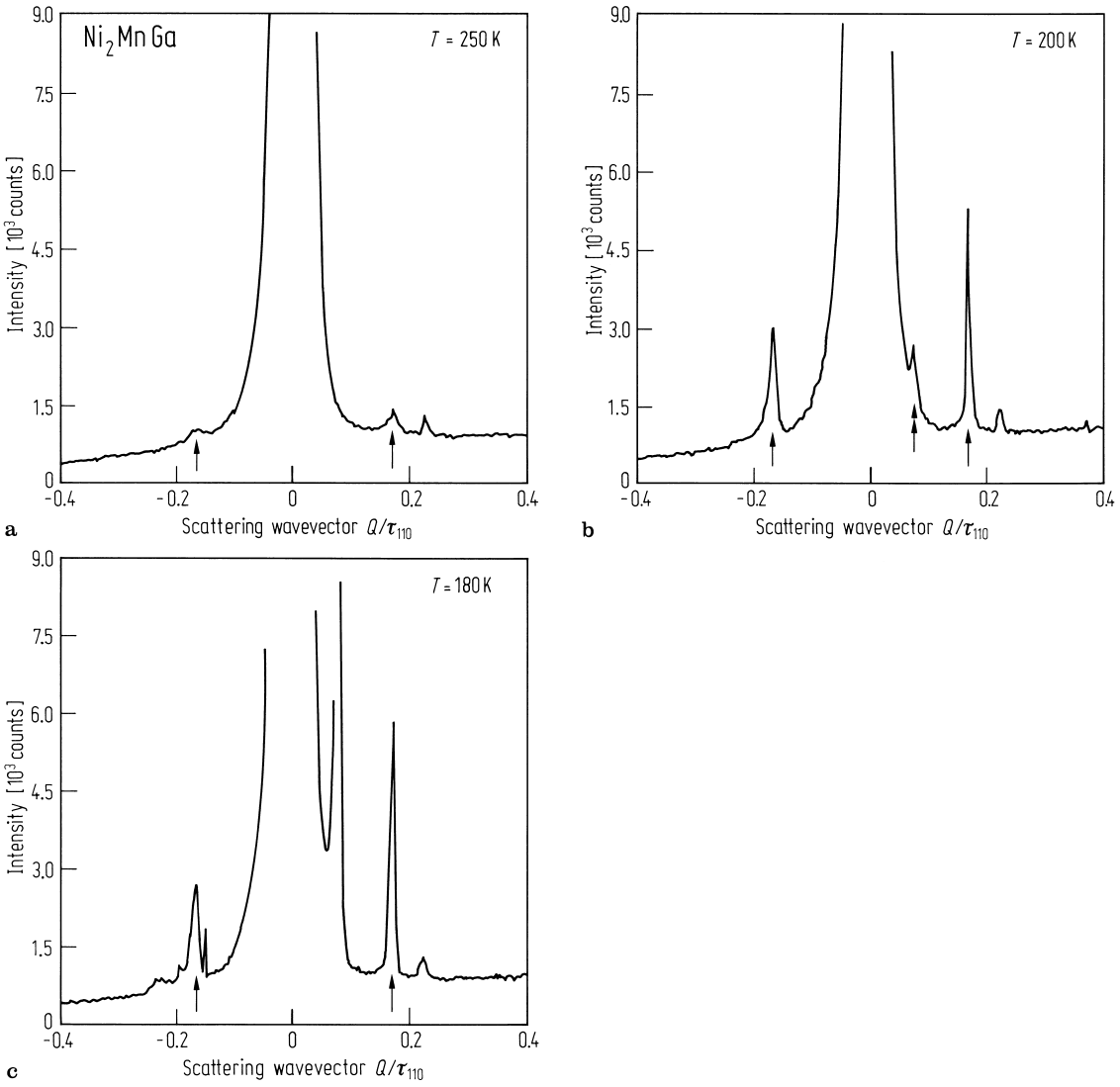

Fig. 250. Temperature dependence of the thermal diffuse X-ray intensity of Ni_2MnGa in the vicinity of the (200) reciprocal lattice vector. The data correspond to the line from the (200) to (310) reciprocal lattice point with the (100) plane as the scattering plane. (**a**) High-temperature phase with the 200 Bragg reflection and two additional peaks at $\pm 0.17\ \tau$ at 250 K; (**b**) at 200 K those additional peaks have increased in magnitude and a Bragg peak of the new phase appears; and (**c**) the same situation at 180 K. The needle-like structure to the right of the peak at $-0.17\ \tau$ is an artefact caused by one data point lying extremely high [94F1].

Atomic disorder caused by cold working reduces the magnetisation without changing the Curie temperature. It has been concluded that this occurs due to an increase in small antiphase domains which couple antiferromagnetically [90K1].

Owing to size effects there are few examples of Heusler alloys forming with actinide elements. Ni_2USn is an exception but it undergoes a structural phase transition at low temperatures.

Valence changes in Heusler alloys containing rare earth elements also give rise to changes in the lattice.

Table 54. A summary of the profile refinement of the diffraction patterns for Pd_2MnSn shown in Fig. 254. A perfectly ordered sample, annealed at 840 °C has a = 6.380 Å, B = 0.16 and a Mn moment of 3.8 μ_B [90K1].

Parameters	As-crushed	Annealed at 300 °C
a [Å]	6.380	6.380
B	0.88	0.85
Average strain		
B_G	$1.03 \cdot 10^{-2}$	$< 1 \cdot 10^{-3}$
A_G	$-2.32 \cdot 10^{-2}$	
B_L	$3.04 \cdot 10^{-2}$	$6.7 \cdot 10^{-3}$
A_L	$-6.33 \cdot 10^{-2}$	$-1.43 \cdot 10^{-2}$
Volume fraction of the cell wall region	40 %	39 %
APB probabilities in the cell wall region	$\alpha_1 = 0.0$ $\alpha_2 = 0.40$	$\alpha_1 = 0.0$ $\alpha_2 = 0.18$
Occupations in the cell wall region		
Pd (¼ ¼ ¼)	1.0	1.0
Mn (0 0 0)	0.7	1.0
Mn (½ ½ ½)	0.3	1.0
Sn (0 0 0)	0.3	1.0
Sn (½ ½ ½)	0.7	1.0

Table 55. A summary of the refinement of the diffraction pattern for Pd_2MnSn shown in Fig. 255. A perfectly ordered sample, annealed at 840 °C has a = 6.360 Å, B = 0.16 and a Mn moment of 3.8 μ_B [90K1].

Parameters	As-crushed	Annealed at 300 °C
a [Å]	6.360	6.360
B	0.23	0.19
Average strain		
B_G	$0.90 \cdot 10^{-2}$	$< 1 \cdot 10^{-3}$
A_G	$-2.08 \cdot 10^{-2}$	
B_L	$2.90 \cdot 10^{-2}$	$6.7 \cdot 10^{-3}$
A_L	$-5.86 \cdot 10^{-2}$	$-1.43 \cdot 10^{-2}$
Magnetic moment of Mn atom [μ_B]		
at Mn site	4.9	4.7
at APB [a])	3 [b])	3.0
at Sn site [c])	4.3	

[a]) Spins at the opposite sides of APB align antiparallel with each other.
[b]) This value is fixed at the same value as that obtained in 300 °C annealed specimen.
[c]) The direction of Mn spins at Sn sites is opposite to those at Mn sites.

Table 56. Pd_2MnSn. Results of magnetisation measurements after annealing at several temperatures [90K1].

	As-crushed	Annealed at			
		300 °C	390 °C	500 °C	800 °C
Θ [K]	178	206	206	207	207
T_C [K]	211	205			201
p_{eff} [μ_B]	4.6	4.9	5.0		5.0
$M_{4\,kOe}$ [G cm^3 g^{-1}] [a])	19	27	40	51	55
$M_{16\,kOe}$ [G cm^3 g^{-1}] [a])	24	33	43	53	56

[a]) Magnetization at 77 K in the magnetic field of 4 and 16 kOe, respectively.

Table 57. Effects of cold working on magnetic properties in several alloys and intermetallic compounds [90K1].

	Structure	Magnitization	T_C
Ni_3Mn	$L1_2$	decrease	decrease
Ni_3Al	$L1_2$	decrease	const
$Ni_{75}Al_{20}Mn_5$	$L1_2$	decrease	decrease
Pt_3Fe	$L1_2$	AF	F
Pt_3Co	$L1_2$	almost const	decrease
$Co_{78}Ti_{22}$	$L1_2$	increase	increase
$Fe_{65}Al_{35}$	$D0_3$	increase	
Pd_2MnSn	$L2_1$	decrease	almost const
Pd_2MnSb	$L2_1$	const	const
Ni_2MnSn	$L2_1$	const	const

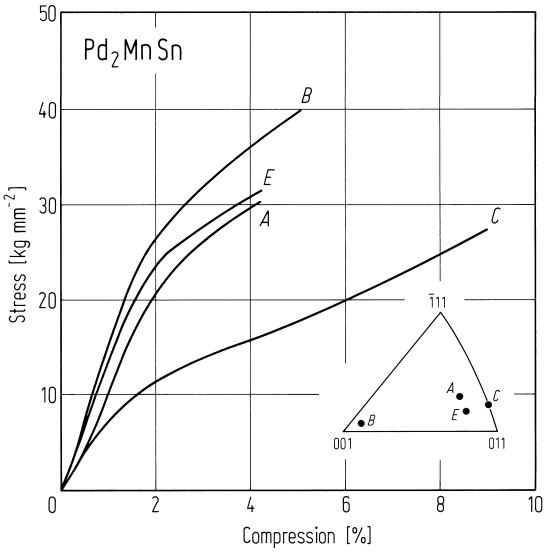

Fig. 252. Stress-strain curves of Pd_2MnSn single crystals with various orientations compressed at room temperature [90K1].

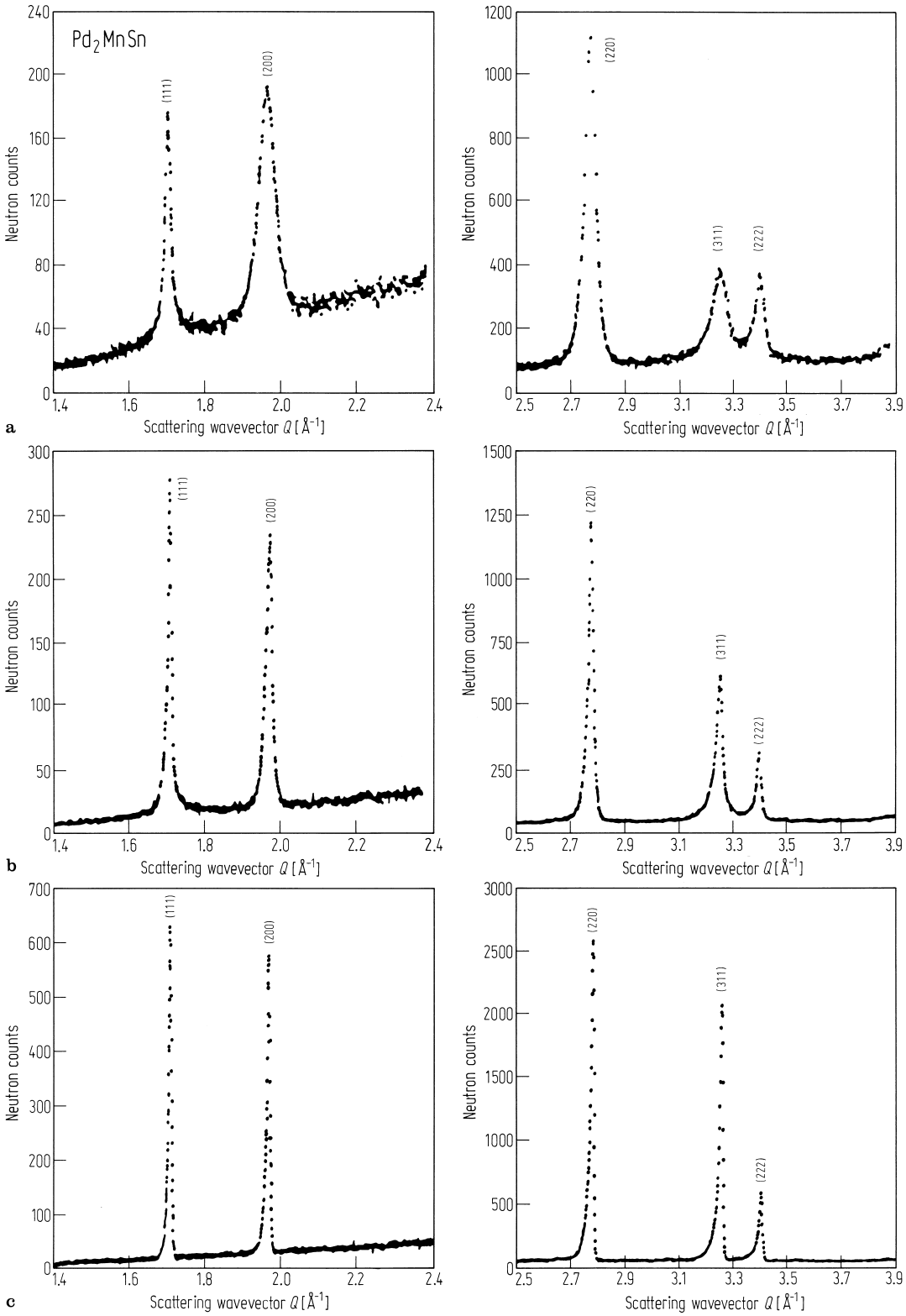

Fig. 253. Neutron diffraction patterns at room temperature of Pd_2MnSn. (**a**) As cold worked, (**b**) cold worked and (**c**) annealed at 300 °C for 12h and at 840 °C for 16h [90K1].

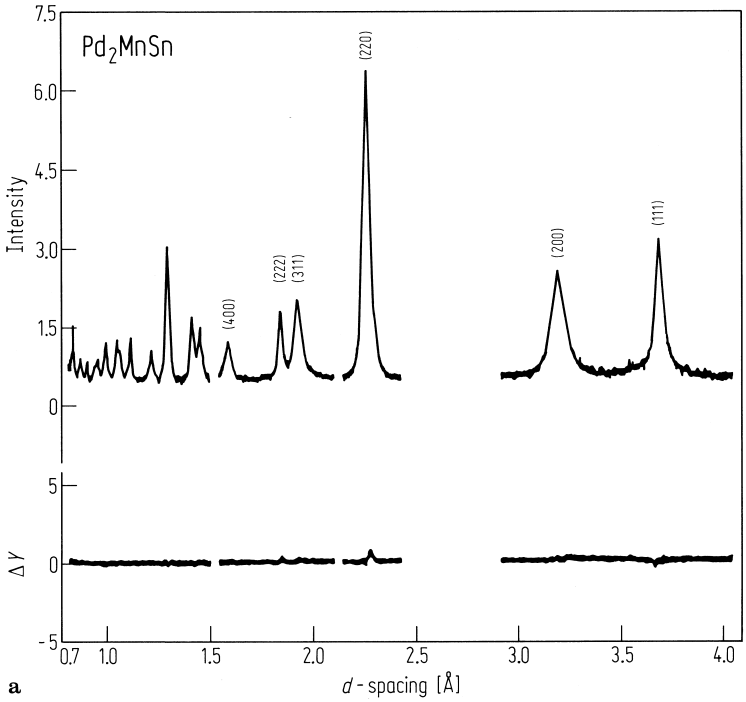

Fig. 254. Profile refinement of the neutron diffraction patterns of Pd_2MnSn shown in Fig. 253. The results are given in Table 54 [90K1].

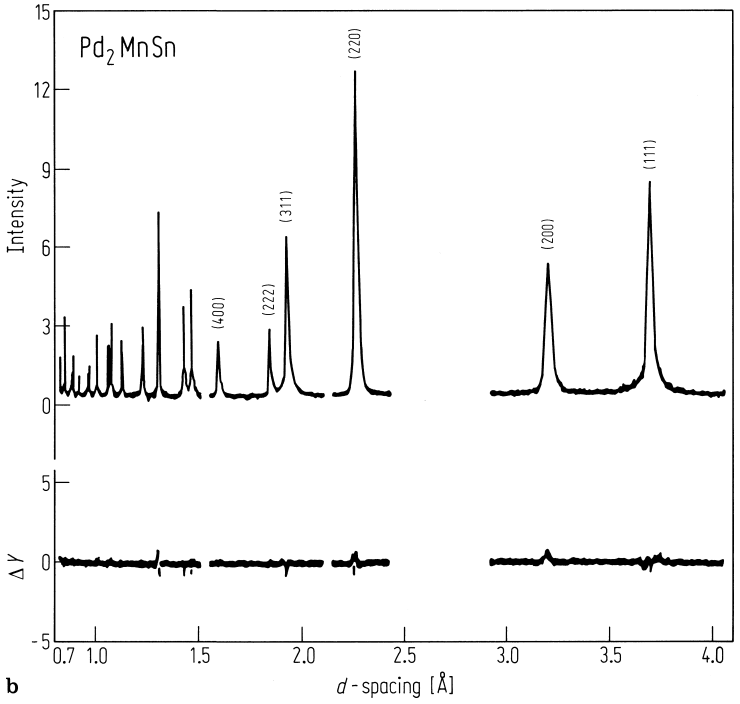

Fig. 254b.

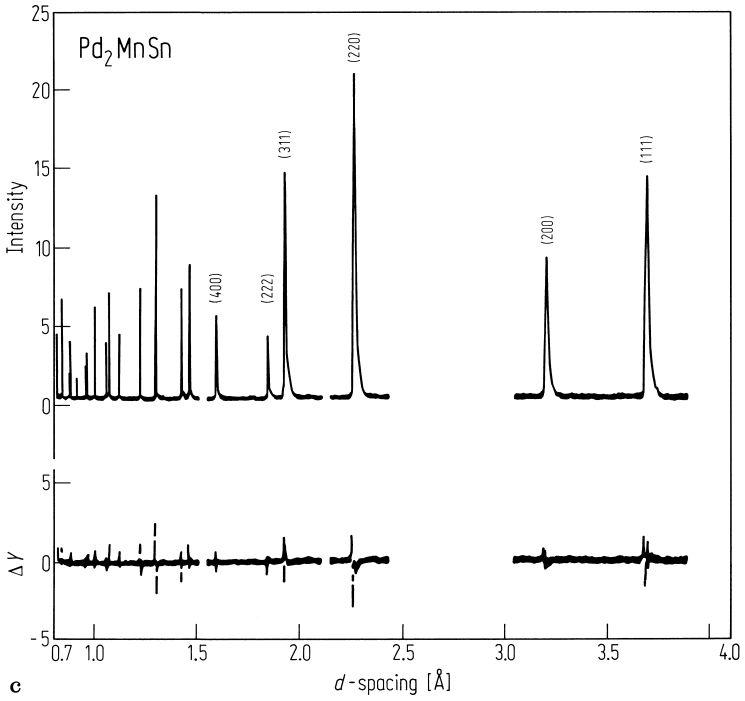

Fig. 254c.

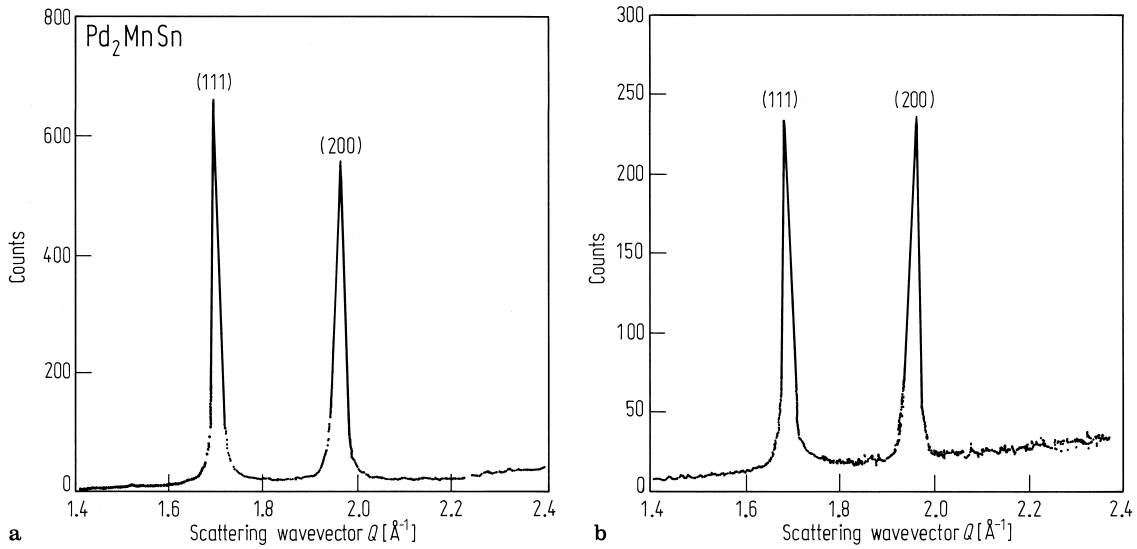

Fig. 255. Neutron diffraction patterns of Pd_2MnSn after 300 °C annealing at (**a**) 40 K and (**b**) room temperature [90K1].

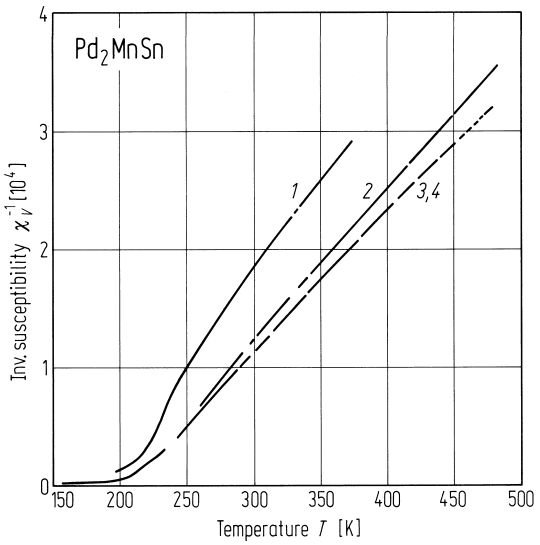

Fig. 256. Temperature dependence of the reciprocal susceptibility of Pd_2MnSn alloys following various heat treatments. (*1*) as-crushed, annealed at (*2*) 300 °C, (*3*) 390 °C, (*4*) 800°C [90K1].

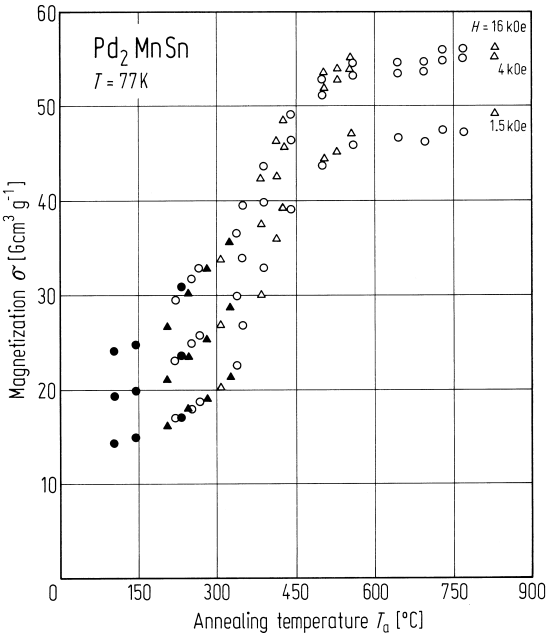

Fig. 257. Recovery of magnetisation of Pd_2MnSn at 77 K in a magnetic field of 1.5, 4 and 16 kOe after heat treatment at various temperatures. The four symbols represent four different samples [90K1].

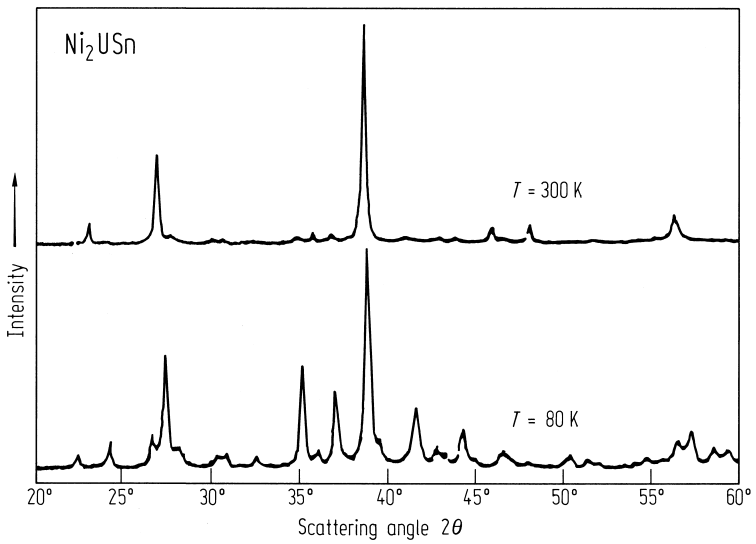

Fig. 258. X-ray diffraction patterns of Ni_2USn at 300 K and at 80 K, i.e. above and below the structural phase transition at 220 K [90E1].

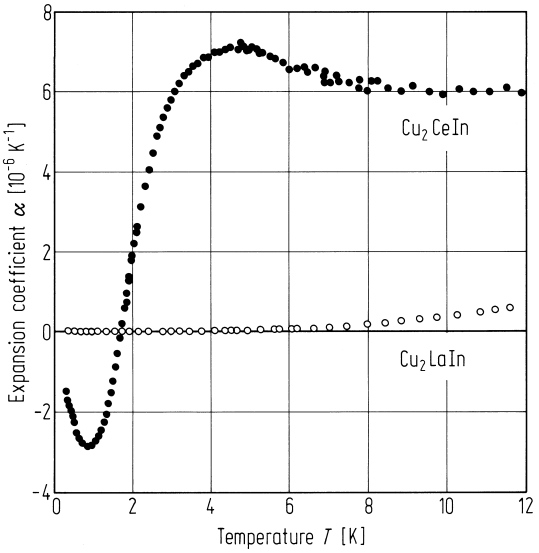

Fig. 259. Coefficient of linear thermal expansion of polycrystalline Cu_2CeIn and Cu_2LaIn [93D1].

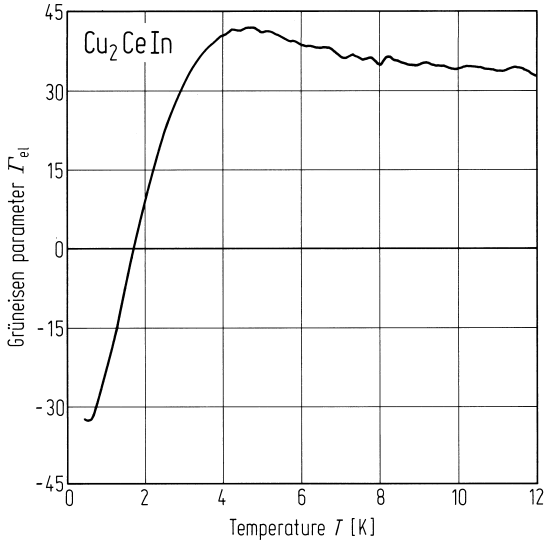

Fig. 260. Electronic Grüneisen parameter of Cu_2CeIn determined assuming an isothermal compressibility K = 1.35 Mbar [93D1].

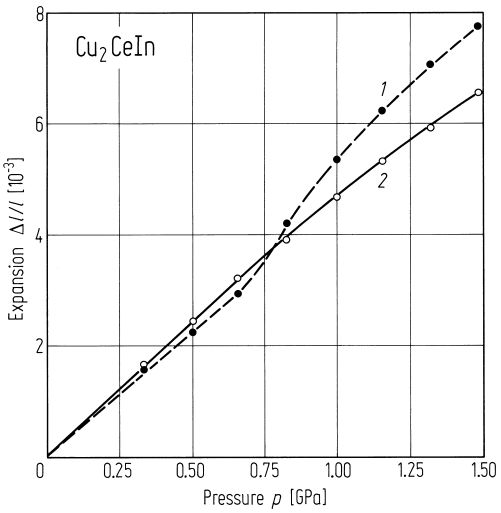

Fig. 261. Relative length change of Cu_2CeIn (*1*) under pressure, compared with that of aluminium (*2*), T = 293 K [87N1].

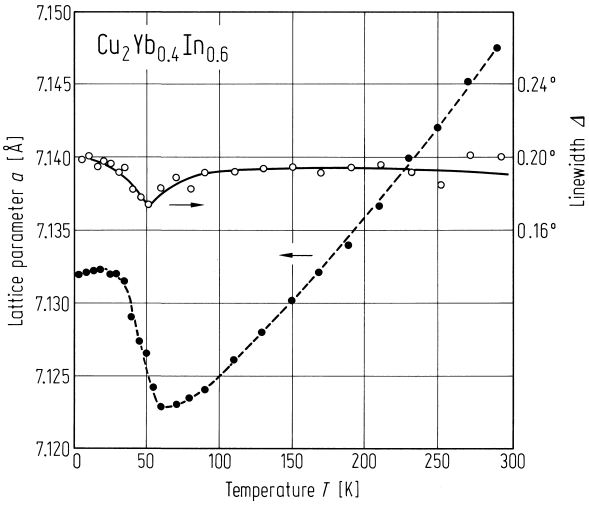

Fig. 262. Temperature dependence of the $Cu_2Yb_{0.4}In_{0.6}$ cubic cell parameter and the X-ray diffraction linewidth Δ of the (422) reflection [87F1].

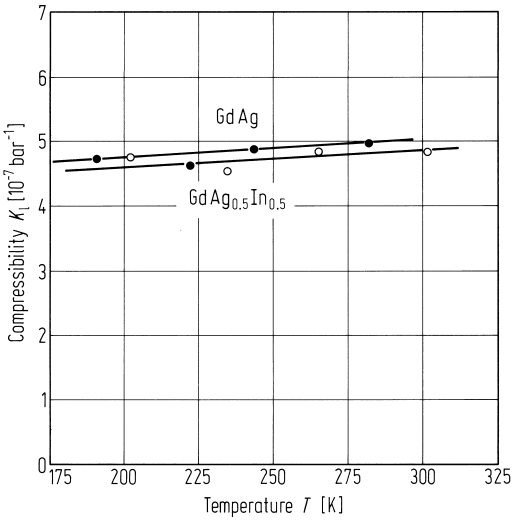

Fig. 263. Temperature dependence of the linear compressibility K_l for $GdAg_{1-x}In_x$ with x = 0 and x = 0.5 [78Y1].

Table 58. Summary of the pressure dependence of the lattice parameter, Curie and Néel temperature of $GdAg_{1-x}In_x$ compounds [78Y1].

x	a_0 [Å]	T_N [K]	T_C [K]	$\Delta T_t/\Delta p$ [10^{-4} K bar^{-1}]	$\partial \ln T_t/\partial \ln V$	K_t at 300 K [10^{-7} bar^{-1}]	$\Delta K_t/\Delta T$ [10^{-10} bar^{-1}K^{-1}]
0	3.648	139.0		0.0	0.0	5.0	3.5
0.10	3.666	131.0		0.0	0.0		
0.15	3.670	116.0		0.0	0.0		
0.20	3.681		24.0	2.5	– 7.9		
0.30	3.688		57.0	4.6	– 6.4		
0.40	3.701		92.9	7.4	– 6.0		
0.50	3.721		111.2	7.6	– 5.2	4.8	3.5

1.5.5.6 Electrical properties

Resistivity measurements have been used to investigate magnetic and structural phase transitions and to establish the onset of superconductivity. Electrical properties of superconductors are reported in subsect. 1.5.5.6.3 dealing with superconductivity.

1.5.5.6.1 Electrical resistivity

The thermal variation of $\rho(T)$ is analysed assuming a residual component ρ_0 indicating sample quality and a temperature dependent metallic contribution $\rho_m(T)$.

$$\rho(T) = \rho_0 + \rho_m(T) \tag{63}$$

A power law dependence is usually used to parameterise $\rho_m(T)$.

$$\rho_m(T) = AT^n \tag{64}$$

The exponent can indicate the type of scattering mechanism. At low temperatures, magnons in a local spin system give rise to n = 2, whereas phonons produce n = 5. An exponent n = 2 is also